AMERICAN JOURNAL OF PHYSIOLOGY
GASTROINTESTINAL AND LIVER PHYSIOLOGY

Am J Physiol Gastrointest Liver Physiol 325: G379–G390, 2023.
First published August 22, 2023; doi:10.1152/ajpgi.00139.2023

METHODS AND RESOURCES

An optimized visualization and quantitative protocol for in-depth evaluation of lymphatic vessel architecture in the liver

Jain Jeong,[1] Masatake Tanaka,[1,2] Yilin Yang,[1] Nikolai Arefyev,[1] Jenna DiRito,[3] Gregory Tietjen,[3] Xuchen Zhang,[4] Matthew J. McConnell,[1] Teruo Utsumi,[1] and Yasuko Iwakiri[1]

[1]*Department of Internal Medicine, Section of Digestive Diseases, Yale University School of Medicine, New Haven, Connecticut, United States;* [2]*Division of Pathophysiology, Medical Institute of Bioregulation and Department of Medicine and Bioregulatory Science, Graduate School of Medical Sciences, Kyushu University, Fukuoka, Japan;* [3]*Department of Surgery, Section of Organ Transplantation and Immunology, Yale University School of Medicine, New Haven, Connecticut, United States; and* [4]*Department of Pathology, Yale University School of Medicine, New Haven, Connecticut, United States*

Abstract

The liver lymphatic system is essential for maintaining tissue fluid balance and immune function. The detailed structure of lymphatic vessels (LVs) in the liver remains to be fully demonstrated. The aim of this study is to reveal LV structures in normal and diseased livers by developing a tissue-clearing and coimmunolabeling protocol optimized for the tissue size and the processing time for three-dimensional (3-D) visualization and quantification of LVs in the liver. We showed that our optimized protocol enables in-depth exploration of lymphatic networks in the liver, consisting of LVs along the portal tract (deep lymphatic system) and within the collagenous Glisson's capsule (superficial lymphatic system) in different species. With this protocol, we have shown 3-D LVs configurations in relation to blood vessels and bile ducts in cholestatic mouse livers, in which LVs were highly dilated and predominantly found around highly proliferating bile ducts and peribiliary vascular plexuses in the portal tract. We also established a quantification method using a 3-D volume-rendering approach. We observed a 1.6-fold ($P < 0.05$) increase in the average diameter of LVs and a 2.4-fold increase ($P < 0.05$) in the average branch number of LVs in cholestatic/fibrotic livers compared with control livers. Furthermore, cholestatic/fibrotic livers showed a 4.3-fold increase ($P < 0.05$) in total volume of LVs compared with control livers. Our optimized protocol and quantification method demonstrate an efficient and simple liver tissue-clearing procedure that allows the comprehensive analysis of liver lymphatic system.

NEW & NOTEWORTHY This article showed a comprehensive 3-D-structural analysis of liver lymphatic vessel (LV) in normal and diseased livers in relation to blood vessels and bile ducts. In addition to the LVs highly localized at the portal tract, we revealed capsular LVs in mouse, rat, and human livers. In cholestatic livers, LVs are significantly increased and dilated compared with normal livers. Our optimized protocol provides detailed spatial information for LVs remodeling in normal and pathological conditions.

cholestasis; fibrosis; liver; lymphatic vessel; tissue-clearing; 3-D imaging

INTRODUCTION

The lymphatic system plays an important role in maintaining tissue fluid balance and immune function. In the liver, the interstitial fluid (lymph) and immune cells are collected by lymphatic capillaries mainly located in the portal tract and subsequently drained into regional lymph nodes and then the thoracic duct. The liver is the largest lymph-producing organ, accounting for 25%–50% of lymph passing through the thoracic duct (1). Studies have reported that aberrant lymphangiogenesis in cirrhotic livers has been implicated in ascites formation, or lymph accumulation, in the peritoneal cavity (1, 2). Despite the significant relevance in liver fibrosis/cirrhosis, the detailed structural alterations of liver lymphatic vessels as well as their alignment with other constituents of the portal tract, such as blood vessels and bile ducts, have not been adequately characterized. Imaging analysis, particularly in three-dimensional (3-D) structure of lymphatic vessels, is crucial for advancing our understanding of the physiology and pathophysiology of the liver. However, lymphatic capillaries are notoriously challenging to visualize because they consist of single thin layers of lymphatic endothelial cells, carry mainly clear lymph fluid, and are difficult to distinguish from nonlymphatic vessels due to a lack of liver lymphatic-specific markers. Although the most complete structural information is gained by 3-D imaging of liver lymphatic vessels, tissue clearing of the liver has presented a barrier to obtaining this information.

In recent years, various tissue-clearing techniques have been developed. One of them is the "Clear, Unobstructed Brain/body Imaging Cocktails and computational analysis (CUBIC),"

Correspondence: Y. Iwakiri (yasuko.iwakiri@yale.edu).
Submitted 7 July 2023 / Revised 11 August 2023 / Accepted 11 August 2023

0193-1857/23 Copyright © 2023 the American Physiological Society.

Downloaded from journals.physiology.org/journal/ajpgi (172.232.036.207) on November 21, 2025.

a method for 3-D tissue staining with tissue clearing, which allows 3-D volumetric analysis for multiple tissues, including brain, kidney, lung, and lymph nodes (3–5). The combination of tissue-clearing techniques with advanced optical techniques (e.g., confocal and light sheet fluorescence microscopy) enables high-throughput imaging of tissues. However, although CUBIC provides excellent clearing performance for many tissues, the method has some technical limitations when applied to the liver. One such limitation is a relatively long immersion time in clearing reagents (6, 7). Since the CUBIC method entails immunostaining of tissues before completing tissue-clearing, a long tissue-clearing time with clearing reagents at high concentrations tends to impair fluorescence signals with certain probes (8). Furthermore, the CUBIC method requires a high temperature during the tissue-clearing process, which also causes fluorescence quenching (9). Thus, the liver still presents a challenge in terms of clearing out tissue contents (e.g., fats, proteins, red blood cells, etc.) for a transparent appearance suitable for 3-D imaging without damaging its structure and losing antigens for immunostaining. Therefore, there exists an unmet need for an optimal protocol for liver tissue-clearing and immunostaining to study challenging aspects of liver anatomy, such as hepatic lymphatic vessels, in 3-D.

This study describes our tissue-clearing protocol with modifications of the CUBIC method to make it more suitable for liver tissue and thus to understand the spatial distribution and structure of hepatic lymphatic vessels in liver diseases. Furthermore, our protocol allows immunostaining with antibodies for colabeling with other constituents of the portal tract. With this protocol, we have shown 3-D lymphatic vessel configurations in relation to blood vessels and bile ducts in biliary fibrotic mouse livers. This protocol allows immunostaining of rat and human livers as well. We have also introduced a quantification method for lymphatic vessels in the liver using immunolabeled 3-D volume-rendering images. This protocol is useful for not only the analysis of hepatic lymphatic vessels but also the analysis of other liver components in normal and pathological conditions.

MATERIALS AND METHODS

Bile Duct Ligation-Induced Liver Injury Model

Endothelial-specific green fluorescent protein mice (EC-GFP reporter mice) were generated by crossing Cdh5-Cre mice (10) and ROSA^{mTmG} mice (Strain No: 007676, The Jackson Laboratory, Bar Harbor, ME). For cre-recombination, EC-GFP reporter mice were injected with tamoxifen (100 mg/kg, Sigma-Aldrich, St. Louis, MO) dissolved in corn oil intraperitoneally for five consecutive days at least 3 wk before the experiment. Male 6- to 10-wk-old, tamoxifen-administrated EC-GFP reporter mice were used for the bile duct ligation (BDL) operation unless otherwise mentioned. BDL or sham (control) operation was performed under anesthesia with ketamine (100 mg/kg) and xylazine (10 mg/kg). In brief, the abdomen was incised, and the common bile duct was separated from surrounding tissues. A 3-0 silk suture was carefully placed in the proximal area of the common bile duct and then ligated with two double knots along the bile duct. For sham-operated mice, the same operation except for the ligation procedure was performed. Livers were collected 4 wk after BDL or sham operation. All animal experiments were approved by the Institutional Animal Care and Use Committee of the Veterans Affairs Connecticut Healthcare System and performed in adherence with the National Institutes of Health *Guide for the Care and Use of Laboratory Animals*.

Human Liver Samples

The liver tissues from four healthy adults from Yale University were used for immunofluorescence experiment. This study was approved by the institutional review board of the authors hospital/institutions and conducted according to the principles of the Declaration of Helsinki. Protocol utilized was HIC#2000027792 (Yale). Written and informed consent was received by the adults used to obtain the liver tissue.

In addition, liver tissue samples were collected from deceased donor organs that were deemed unsuitable for transplantation and subsequently allocated for research purposes. All organs were recovered for research following strict ethical guidelines and standard practices at New England Donor Services (NEDS), the Organ Procurement Organization responsible for the New England Region. Consent for the use of the organs for research was obtained from the donor family by NEDS representatives before organ retrieval.

3-D Immunofluorescence Imaging

We optimized a tissue-clearing procedure for liver 3-D imaging by modifying the CUBIC tissue-clearing method (4) and applied it to livers from normal (C57BL/6J), sham-operated, and 4-wk BDL mice (EC-GFP reporter mice). Detailed procedures are presented in the Supplementary Extended Procedure of the Supplemental Material. Briefly, mice were euthanized under anesthesia with whole livers isolated, from which large lobes (left lateral lobes) and small lobes (right lobes) were harvested. Normal human liver tissues were obtained through donation after circulatory death (DCD) and cut into small pieces [height (H):width (W):depth (D) = 8 mm × 12 mm × 4 mm]. Both mouse and human liver tissue samples were washed with PBS and fixed in 4% paraformaldehyde (PFA) at 4°C for 24 h. The fixed samples were washed with washing buffer A [PBS containing 0.01% (wt/vol) sodium azide (Sigma-Aldrich)] at room temperature for 2 h, then at 4°C overnight, and again at room temperature for 2 h. The samples were then cleared with water-diluted CUBIC reagent-1 [mix of equal volumes of ddH_2O and CUBIC reagent-1, 25% (wt/wt) urea (Sigma-Aldrich), 25% (wt/wt) Quadrol (Sigma-Aldrich), 15% (wt/wt) triton X-100 (AmericanBio, Canton, MA), and 35% (wt/wt) ddH_2O] at 37°C for 6 h and then with only CUBIC reagent-1 at 37°C for ~8 days. For further tissue clearing, the samples were washed with washing buffer A at room temperature for 2 h, then at 4°C overnight, and again at room temperature for 2 h. The samples were then immersed in PBS-diluted CUBIC reagent-2 [mix of equal volumes of PBS and CUBIC reagent-2, 25% (wt/wt) urea, 50% (wt/wt) sucrose, 10% (wt/wt) triethanolamine (DOT Scientific, Burton, MI), and 15% (wt/wt) ddH_2O] at 37°C overnight and then in only CUBIC reagent-2 at 37°C for ~8 days.

Before immunostaining for 3-D imaging to remove CUBIC reagent-2 completely, the cleared samples were thoroughly washed with washing buffer A at room temperature for 2 h, then

Downloaded from journals.physiology.org/journal/ajpgi (172.232.036.207) on November 21, 2025.

at 4°C overnight, and again at room temperature for 2 h. The washed samples were cut into small pieces with ≤3-mm thickness (Fig. 1*J*, *step 4*). The samples were then incubated at 4°C overnight in blocking buffer [PBS containing 0.01% sodium azide, 1% (vol/vol) triton-X100, and 5% (vol/vol) donkey serum], followed by incubation with primary antibodies including rabbit anti-LYVE1 (1:200, ab14917, Abcam, Cambridge, UK) (11), goat anti-αSMA (1:200, NB300-978, Novus Biologicals, Centennial, CO) (12), rat anti-CK19 (1:25, TROMA-III, DSHB, Iowa City, IA) (13), rabbit anti-CK19 [1:100, 10712-1-AP, Proteintech (Rosemont, IL)] (14), mouse anti-hPDPN (1:100, M3619, Dako, Santa Clara, CA) (15), and rabbit anti-αSMA (1:200, ab124964, Abcam) (16) (see Table 1). Blocking buffer was used as a diluent for the primary antibodies. After incubation with the primary antibodies, the samples were washed three times with washing buffer B (PBS containing 1% sodium azide and 0.1% triton-X100) at room temperature for 1 h, followed by incubation with donkey anti-rabbit Alexa 647 (1:300, A31573, Invitrogen, Waltham, MA), donkey anti-goat Alexa 488 (1:300, A11055, Invitrogen), donkey anti-rat Alexa 555 (1:300, A48270, Invitrogen), donkey anti-mouse Alexa 647 (1:300, A31571, Invitrogen), and donkey anti-rabbit Alexa 488 (1:300, A21206, Invitrogen) secondary antibodies at 4°C for 3 days with blocking buffer as a diluent. Finally, the samples were washed with washing buffer B three times at room temperature for 1 h, followed by incubation in CUBIC reagent-2 at room temperature for 1 day for further tissue-clearing (Fig. 1, *step 7*). The samples were placed on a microscope sample holder for *z*-scanning imaging on the *xy*-motorized stage in a confocal microscope (TCS SP5 confocal microscope, Leica, Wetzlar, Germany) (Fig. 1*M*, *step 8*). *Z*-stack images were acquired as 16-bit images with a pixel resolution of 512 × 512 or 1,024 × 1,024 (for human capsular lymphatics). Confocal microscope parameters and detailed information of images are presented in Figure legends and the Supplementary Extended Procedure.

3-D Volume-Rendering Analysis

Z-stack images were corrected and deconvolved using the Classic Maximum Likelihood Estimation (CMLE) algorithm

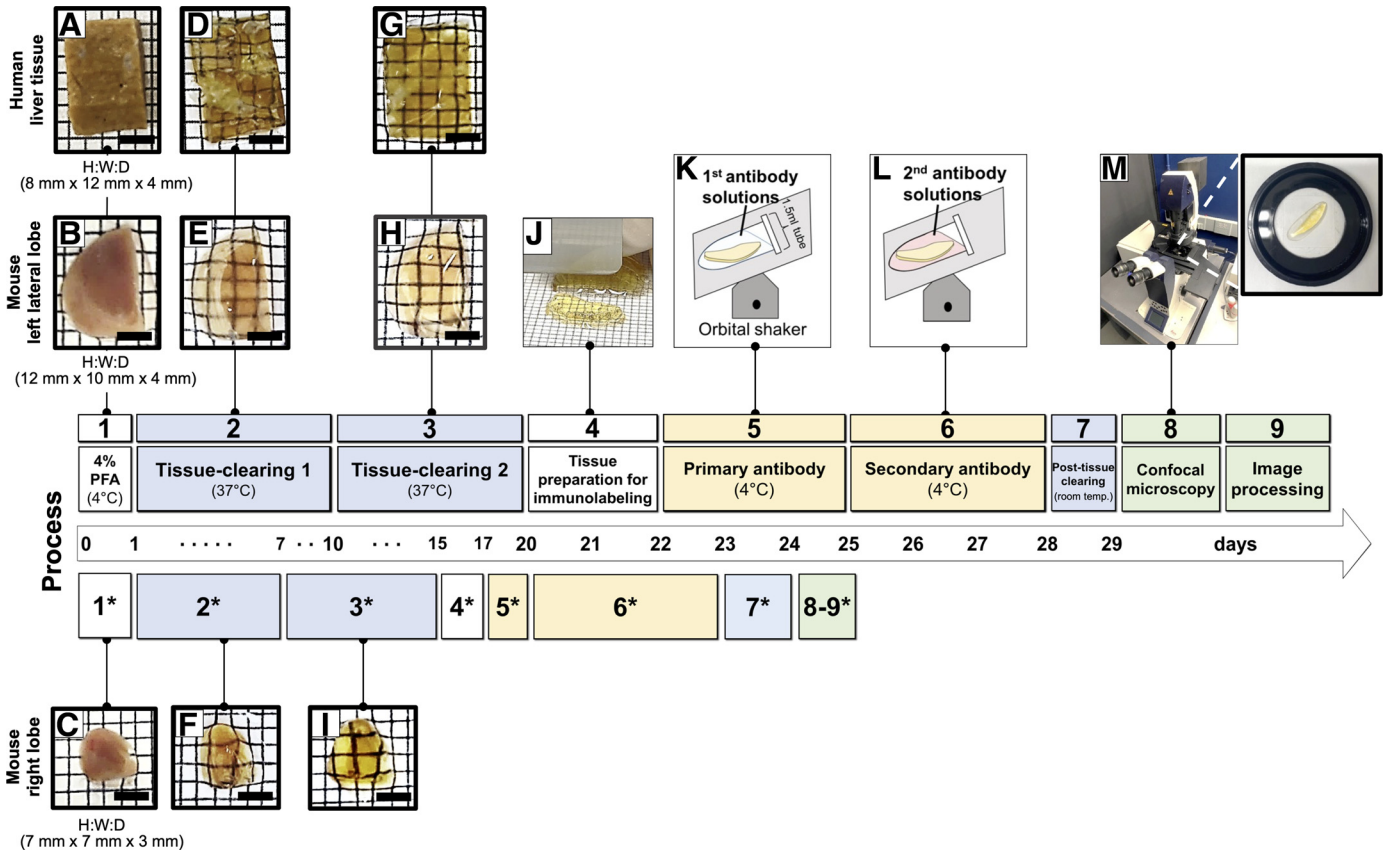

Figure 1. Overview of our modified CUBIC tissue-clearing method in human and mouse liver tissues. Our modified CUBIC method includes three major processes, which are tissue-clearing (blue boxes), immunostaining (yellow boxes), and image acquisition (green boxes). For mouse livers, two versions are presented according to liver lobe sizes, which differ in clearing periods. Human liver tissue [large lobe, height (H):width (W):depth (D) = 8 mm × 12 mm × 4 mm] (*A*), mouse left lateral lobe (large lobe, H:W:D = 12 mm × 10 mm × 4 mm) (*B*), and mouse right lobe (small lobe, H:W:D = 7 mm × 7 mm × 3 mm) (*C*) were fixed in 4% PFA. Human liver tissue (*D*) and mouse large lobe (*E*) were treated with CUBIC reagent-1 for 9 days. *F*: mouse small lobe was treated with CUBIC reagent-1 for 6 days. For further clearing, human liver tissue (*G*) and mouse large lobe (*H*) were treated with CUBIC reagent-2 for 10 days, whereas mouse small lobe (*I*) was treated for 8 days. It took a total of 19 days to have human liver tissue and mouse large lobe fully cleared and 14 days for mouse small lobe. *J*: after tissue clearing, human liver tissue and mouse liver lobes were sectioned to small pieces with ≤3-mm thickness to increase antibody permeability. *K* and *L*: immunostaining was performed with primary and secondary antibodies for 3 days each (total 6 days), followed by an additional 1 day of postimmunostaining tissue-clearing (*step 7*). *M*: for imaging, immunostained liver tissues were placed in a microscope sample holder on the microscopic *xy* stage and scanned with a confocal microscope. Three-dimensional (3-D) reconstruction and volume rendering were performed with Imaris and Huygens software. Asterisk marks are added to the processes for mouse small lobe. Scale bars: 4 mm. CUBIC, Clear, Unobstructed Brain/body Imaging Cocktails and computational analysis.

Downloaded from journals.physiology.org/journal/ajpgi (172.232.036.207) on November 21, 2025.

Table 1. *Antibody list*

Antibody	Company	Cat. No.	Source	Dilution	Target Tissue	Usage	
						2-D	3-D
mLYVE1	Abcam	ab14917	Rabbit polyclonal	1:200	Mouse liver	O	O
mLYVE1	R&D Systems	AF2125	Goat polyclonal	1:200	Mouse liver		O
ratLYVE1	R&D Systems	AF7939	Sheep polyclonal	1:100	Rat liver	O	
hPDPN	Dako	M3619	Mouse monoclonal	1:100	Human liver	O	O
CK19	Developmental Studies Hybridoma Bank (DSHB)	TROMA-III	Rat monoclonal	1:25	Mouse liver		O
CK19	Proteintech	10712-1-AP	Rabbit polyclonal	1:100	Human liver		O
αSMA	Novus Biologicals	NB300-978	Goat polyclonal	1:200	Mouse liver		O
αSMA	Abcam	ab124964	Rabbit monoclonal	1:200	Human liver		O
Col-I	Abcam	ab292	Rabbit polyclonal	1:100	Human, mouse, Rat liver	O	

All secondary fluorescent conjugated secondary antibodies were used with a dilution of 1:300.

in Huygens professional software and mounted into Imaris software for 3-D reconstruction. Volume rendering of GFP, LYVE1, PDPN, CK19, and αSMA positive structures was conducted based on absolute fluorescence intensities, and thresholds were adjusted manually to isolate lymphatic vessel, blood vessel, and ductular structures. For quantification of lymphatic vessels with a focus on the portal tract, we used at least three cleared liver sections (≤3-mm thickness) from the large lobe (left lateral lobe) per mouse (see Fig. 5). Lymphatic vascular parameters were obtained using the "surface" volume rendering and "filament tracer" tools in Imaris. Briefly, the "surface" volume-rendering tool allows us to quantify the total volume of LYVE1-positive lymphatic vessels. Volume rendering was performed based on labeled fluorescence intensities (Fig. 5*A*), and thresholds were manually adjusted (Fig. 5*B*). Rendered LYVE1-positive lymphatic vessels were visually checked to confirm proper vascular connections. Particularly, LYVE1-positive lymphatic vessels connected with LYVE1-positive liver sinusoidal endothelium were manually removed (Fig. 5*C*). The "filament tracer" tool was used to quantify the vessel diameters and branch numbers. The algorithm in the "filament tracer" tool was set for automatic filament and path detection based on target fluorescence (Fig. 5*D*), and thresholds were manually adjusted (Fig. 5*E*). Rendered LYVE1-positive lymphatic vessels by the "filament tracer" tool were visually checked to ensure proper vascular connections (Fig. 5*F*). All data were exported to Excel files for further analysis.

2-D Conventional Immunofluorescence Imaging

Paraffin-embedded liver tissue blocks were sectioned by 7-μm thickness. Sectioned liver slides were deparaffinized with xylene and rehydrated with decreasing concentrations of ethanol. Antigen retrieval was performed by preheating the liver slides in 10 mM sodium citrate buffer (pH 6.0) for 30 s in a microwave oven, followed by incubation in a steamer for 15 min and cooling at room temperature for 20 min. The liver slides were washed with PBS and incubated in blocking buffer (PBS containing 5% donkey serum and 0.3% triton X-100) at room temperature for 1 h. After blocking was completed, the liver slides were incubated with goat anti-mouse LYVE1 (1:200, AF2125, R&D Systems, Minneapolis, MN) (17), sheep anti-rat LYVE1 (1:100, AF7939, R&D Systems) (18), and rabbit anti-COL-I (1:100, ab292, Abcam) (19) primary antibodies at 4°C overnight, followed by washing with PBS for 5 min for 3 times and incubation with secondary antibodies including donkey anti-goat Alexa 647 (1:300, A32849, Invitrogen), donkey anti-sheep Alexa 647 (1:300, A21448, Invitrogen), and donkey anti-rabbit Alexa 488 at room temperature for 30 min. For immunostaining of PDPN in human liver slides, we amplified fluorescence signal using the avidin-biotin amplification method (SP-2001, Vector Laboratories, Newark, CA). The human slides were incubated with mouse anti-hPDPN (1:100, M3619, Dako) primary antibody at 4°C overnight, followed by being washed three times with PBS at room temperature for 5 min. The slides were incubated with biotinylated anti-mouse IgG (1:300, BA-9100, Vector Laboratories) at room temperature for 30 min and then with secondary Alexa Fluor 647 streptavidin (1:300, S21374, Invitrogen) at room temperature for 30 min. Finally, the human liver slides were washed three times with PBS for 5 min and mounted with Fluoroshield containing DAPI (Sigma-Aldrich). Images were obtained using a fluorescence microscope (Zeiss Axio Observer Z1, Zeiss, Oberkochen, Germany).

Quantification of Lymphatic Vessel Numbers and Areas by 2-D Conventional Immunofluorescence Imaging

Deparaffinization, antigen retrieval, and blocking were conducted as described above in the 2-D conventional Immunofluorescence imaging section. After blocking was completed the liver slides were incubated with rabbit anti-LYVE1 (1:200, ab14917, Abcam) primary antibody at 4°C overnight, followed by being washed three times with PBS for 5 min and incubation with donkey anti-rabbit Alexa 647 secondary antibody at room temperature for 30 min. Thirteen to sixteen images of the portal tract were randomly taken at ×200 magnification per slide. LYVE1-positive lymphatic vessel numbers and areas were measured by ImageJ (NIH).

Quantification of Capsular Thickness in Human, Mouse, and Rat Livers by Sirius Red Staining

For measurement of liver capsular thickness, Sirius Red staining was performed on formalin-fixed paraffin-embedded liver tissues. Paraffin sections (7-μm thickness) were deparaffinized with xylene, rehydrated with decreasing concentrations of ethanol, and stained with picro-sirius red (F3B, Direct Red 80, 36-554-8, Sigma-Aldrich) for 1 h, and washed by 10 dips into 0.5% acetic acid (glacial) solution (acetic acid, glacial, 14-650-388, J.T.Baker, Thermo Fisher Scientific, Waltham, MA) two times, followed by dehydration with increasing concentrations of ethanol and clearing with xylene. Five to ten images of the

Downloaded from journals.physiology.org/journal/ajpgi (172.232.036.207) on November 21, 2025.

liver capsular area were taken per slide using the Olympus BX51 fluorescence microscope with a ×4 objective lens. Image J was used for quantification of the liver capsular area. The green channel was separated from the image using the RGB stack option, and an appropriate threshold was applied. Then, the liver capsular area was selected using the "polygon selection" tool, and the Sirius Red positive area in the selected area was measured using the "measure" tool. The length of the capsular area was measured using the "segmented line" tool. The thickness of the capsule was determined by dividing the Sirius Red positive capsular area by the length of the capsular area.

Statistical Analysis

Based on our published studies (20–31) and preliminary studies, the desirable sample size (32) for histological analyses of mouse samples is 6–10 mice per group. This sample size will be adequately powered to generate significant results. All data are expressed as means ± SE. A comparison between the two groups was performed using the unpaired Student's *t* test. A comparison among multiple groups was performed using the one-way ANOVA. A *P* value of <0.05 was considered statistically significant.

RESULTS

Tissue-Clearing Procedures for the Human and Mouse Livers Using a Modified CUBIC Method

We established a modified CUBIC tissue-clearing method, which allowed us to visualize the structure of lymphatic vessels and other components such as blood vessels and bile ducts in the human and mouse livers with immunostaining and confocal microscopy. We also optimized immunostaining procedures to improve immunofluorescence signal and antibody permeability, which enabled us to analyze spatial alterations of these components in fibrotic livers, including their quantifications, in combination with a 3-D volume-rendering approach. Steps and time courses of the clearing process are presented in Fig. 1.

We first compared the tissue-clearing efficiency for livers from different species (human and mouse) or with different sizes using our modified CUBIC tissue-clearing method. We used 4% PFA-fixed human liver tissue (H:W:D = 8 mm × 12 mm × 4 mm), mouse large lobe (left lateral lobe, H:W:D = 12 mm × 10 mm × 4 mm), and small lobe (right lobe, H:W:D = 7 mm × 7 mm × 3 mm) (Fig. 1*A–C*, respectively, *step 1*). Human liver tissue, mouse large lobe, and small lobe started to become transparent under treatment with CUBIC reagent-1 (Fig. 1, *D–F*, *step 2*), and got fully transparent after being treated with CUBIC reagent-2 (Fig. 1, *G–I*, *step 3*). It took 19 days to have human liver tissue and mouse large lobe fully cleared, and 14 days for mouse small lobe. We then sectioned these liver tissues into small pieces with ≤3-mm thickness before immunostaining to increase antibody permeability (Fig. 1*J*, *step 4*). The most optimal thickness was 2–3 mm for the immunostaining process (6 days) with primary and secondary antibodies (Fig. 1, *steps 5* and *6*). While the original CUBIC method described immunostaining during the tissue-clearing process (3), we performed immunostaining on fully cleared liver tissues to preserve an intact fluorescence signal (Fig. 1, *K* and *L*, *steps 5* and *6*), followed by1-day post-tissue-clearing (Fig. 1, *step 7*).

3-D Visualization of Lymphatic Vessels and Other Components in the Portal Tract of Normal Mouse and Human Livers

To visualize lymphatic vessels and other components such as blood vessels and bile ducts, we performed immunostaining with LYVE1, PDPN, αSMA, and CK19 antibodies (markers for lymphatic vessels, blood vessels, and bile ducts, respectively). After immunostaining, we imaged liver tissues by confocal microscopy (Fig. 1*M*). As shown in Fig. 2, *A–C*, reconstructed 3-D images successfully visualized 3-D structure of LYVE1- or PDPN-positive lymphatic vessels (LVs) along with αSMA-positive portal vein (PV) and CK19-positive bile ducts (BDs) in the portal tract of normal mouse and human livers in details. We were able to observe lymphatic vessel structure at a depth of at least 350 μm in the liver tissues cleared and processed by our modified CUBIC method. A 3-D volumetric approach also allowed us to see lymphatic vessels running alongside bile ducts in the portal tract (Fig. 2, *A* and *C*, *right*).

Lymphatic Vessels in the Capsular Area of Normal Human, Mouse, and Rat Livers

It is thought that around 80% of the lymph produced by the liver flows into lymphatic vessels in the portal tract, while the remaining lymph is drained into lymphatic vessels in the capsular area (1). Therefore, we also investigated structural features of lymphatic vessels in the capsular area of normal human, mouse, and rat livers. Our Sirius Red staining of the capsular area, which mainly stained the collagenous capsular area (Fig. 3*A*), revealed that the human capsular area was significantly thicker than either the mouse or rat capsular area ($P = 0.020$ and $P = 0.031$, respectively). Our 2-D conventional histological analysis of immunostaining with PDPN or LYVE1 antibody along with Col-I (a marker of the collagenous capsular area) antibody showed abundant capsular lymphatic vessels inside the Col-I positive collagenous capsular area in human liver tissue, while fine structure of capsular lymphatic vessels was not observed in either the normal mouse or rat liver (Fig. 3*B*). To assess human capsular lymphatics in 3-D, we isolated the surface of liver tissue (Fig. 3*C*, *top*) covered by the thin collagenous capsule area (Glisson's capsule) (Fig. 3*C*, *bottom*) and visualized lymphatic vessels by immunostaining with PDPN following tissue-clearing (Fig. 3*D*, *left* and Supplementary Movie S1). 3-D volume rendering confirmed abundant capsular lymphatic vessels forming a structurally well-organized network (Fig. 3*D*, *right*).

3-D Structural Analysis of Lymphatic Vessels and Their Spatial Relationship with Bile Ducts and Blood Vessels in Normal and Biliary Cirrhotic Mouse Livers

For 3-D structural analysis of lymphatic vessels, we used liver tissues from endothelial cell (EC)-specific GFP reporter mice, in which GFP is expressed in all types of ECs, allowing us to view an entire landscape of the liver vasculature. To determine whether alterations of lymphatic vessels occurred in biliary cirrhotic livers, we performed immunostaining of LYVE1 in the livers of sham-operated mice and biliary cirrhotic mice with bile duct ligation (BDL) for 4 wk (Fig. 4, *A* and *B*). BDL induces obstructive cholestatic injury and

Downloaded from journals.physiology.org/journal/ajpgi (172.232.036.207) on November 21, 2025.

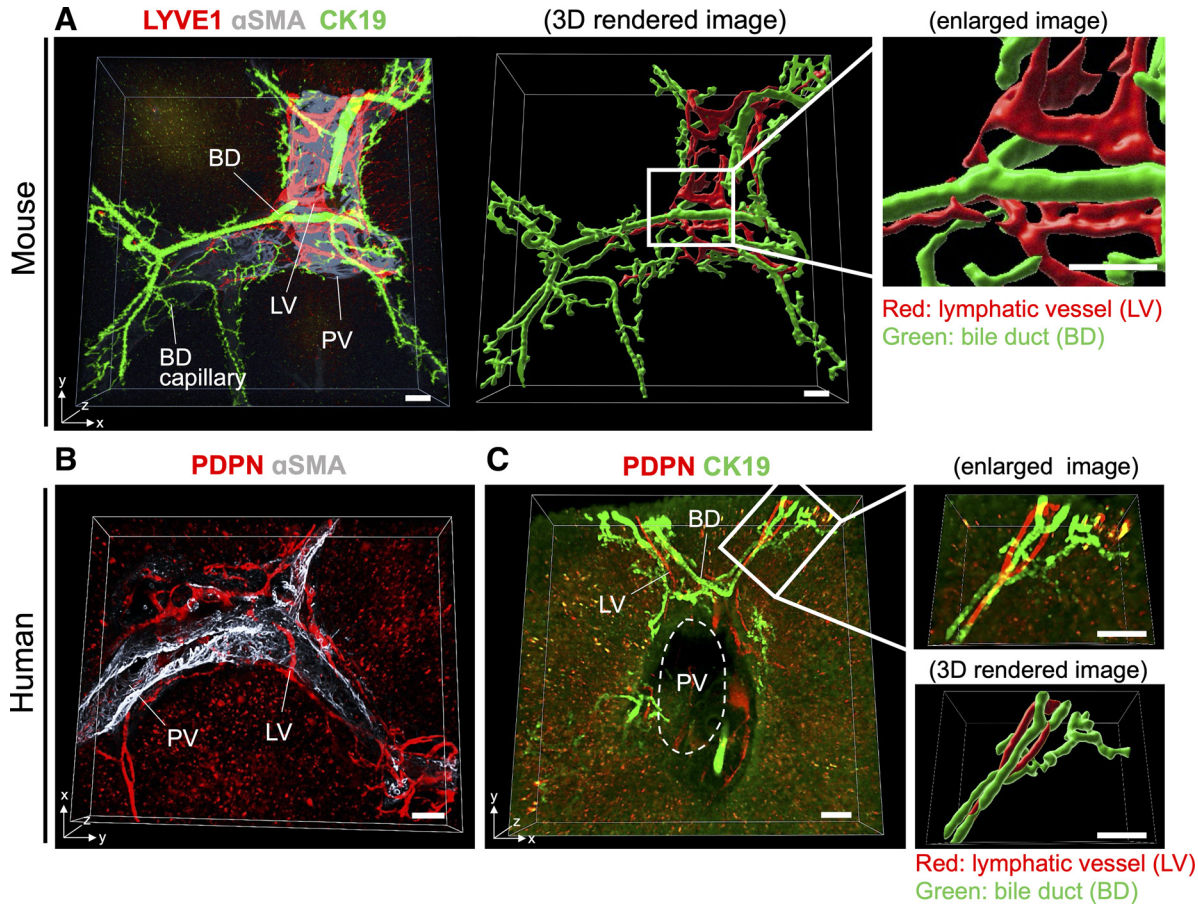

Figure 2. Three-dimensional (3-D) visualization of lymphatic vessels in the portal tract of normal mouse and human livers. *A, left*: reconstructed 3-D image of the portal tract in the normal mouse liver. Imaging condition: *z*-step size = 0.4 μm, image volume [*x*] × [*y*] × [*z*] = 1,290 μm × 1,290 μm × 354 μm. Liver tissue was cleared and stained with LYVE1 (red, lymphatic vessel), αSMA (white, portal vein), and CK19 (green, bile duct) antibodies. *Right*: 3-D volume-rendering image of lymphatic vessels and bile ducts using Imaris software with an enlarged image. Scale bars: 100 μm. *B*: reconstructed 3-D image of the portal tract in normal human liver tissue. Imaging condition: *z*-step size = 0.4 μm, image volume [*x*] × [*y*] × [*z*] = 1,002 μm × 1,168 μm × 228 μm. Liver tissue was cleared and stained with PDPN (red, lymphatic vessel) and αSMA (white, portal vein) antibodies. Scale bar: 100 μm. *C*, left: reconstructed 3-D image of the portal tract in normal human liver tissue. Imaging condition: *z*-step size = 0.4 μm, image volume [*x*] × [*y*] × [*z*] = 1,193 μm × 1,193 μm × 233 μm. Liver tissue was cleared and stained with PDPN (red, lymphatic vessel) and CK19 (green, bile duct) antibodies. *Right*, *top*: enlarged reconstructed 3-D image. *Right*, *bottom*: 3-D volume-rendering image. Scale bars: 100 μm.

extensive proliferation of bile ducts (ductular reaction) (33). The peribiliary vascular plexus (PBP), a network of small hepatic arteries distributed in the intra- and extra-hepatic bile duct walls, also undergoes extensive proliferation to support increased nutritional and functional needs of the proliferating bile ducts (34). Our immunostaining in biliary cirrhotic livers showed that lymphatic vessels were highly dilated and predominantly found around highly proliferating bile ducts and PBPs in the portal tract with their number significantly increased (Fig. 4*B*). Furthermore, 3-D volume rendering demonstrated that PBPs were mostly located around intrahepatic bile ducts (Fig. 4, *D* and *E*) and covered by highly dilatated lymphatic vessels (Fig. 4*F*), suggesting possible crosstalk between proliferating lymphatic vessels, bile ducts, and PBPs in biliary cirrhotic livers.

Quantification of Lymphatic Vessels: 3-D versus 2-D Analysis

Using a computational 3-D volume-rendering approach, we quantified LV parameters (diameter, branch number, and total volume) with Imaris 3-D rendering tools (Surface and Filament Tracer) (Fig. 5) in the portal tract of sham and BDL mouse livers (Fig. 6, *A* and *B*). We found that the average diameter of lymphatic vessels increased 1.6-fold ($P = 0.038$) in BDL livers (33.8 μm ± 2.9) compared with sham livers (21.1 μm ± 2.1). Likewise, BDL livers increased the average branch number of lymphatic vessels 2.4-fold ($P = 0.012$, 21.5 ± 2.9 vs. 9.0 ± 1.7) and the average total volume 4.3-fold ($P = 0.05$, 5.4 ± 1.8 × 10^6 μm^3 vs. 1.2 ± 0.5 × 10^6 μm^3) (Fig. 6*C*). These results demonstrate large alterations in the network of hepatic lymphatic vessels due to biliary cirrhosis.

We then measured similar parameters (diameter, number, and total area) in conventional 2-D images using 7-μm thick liver section slides to compare results with those from 3-D images (Fig. 6*D*). Results from 2-D images also showed significant increases in all parameters of lymphatic vessels in BDL livers compared with sham livers (Fig. 6*E*). The average lymphatic vessel diameters in BDL and sham livers in 2-D analysis were 40.5 μm ± 4.3 and 25.5 μm ± 2.6 ($P = 0.014$, 1.6-fold), respectively, while the respective average lymphatic vessel numbers were 5.4 ± 0.3 and 2.9 ± 0.5 ($P = 0.002$, 1.9-fold). Unique differences between 2-D and 3-D quantification are

Downloaded from journals.physiology.org/journal/ajpgi (172.232.036.207) on November 21, 2025.

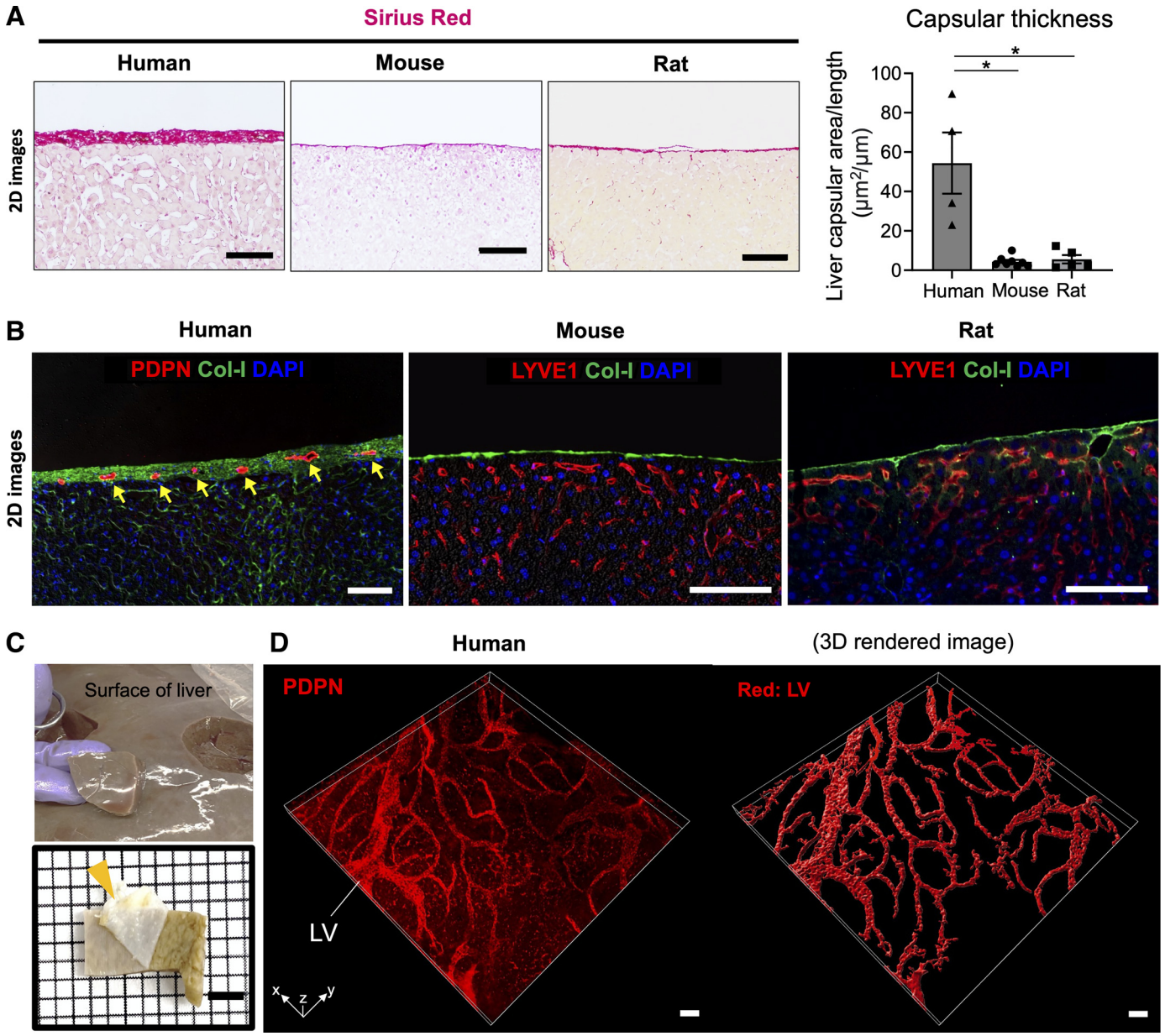

Figure 3. Lymphatic vessels in the capsular area of normal mouse, rat, and human livers. *A*: comparison of the capsular areas (thickness) among normal human ($n = 4$), mouse ($n = 7$), and rat livers ($n = 7$) stained with Sirius Red. Scale bars: 100 μm. *B*: two-dimensional (2-D) conventional histology images of the capsular areas (paraffin section, 7-μm thickness) from normal human, mouse, and rat livers stained with PDPN or LYVE1 (red, lymphatic vessel) and Col-I (green, collagenous capsular area), respectively. Yellow arrows indicate lymphatic vessels inside the Col-I positive capsular area. 2-D images were merged with differential interference contrast (DIC) images. Scale bars: 100 μm. *C*: surface of human liver tissue (*top*) covered by thin collagenous capsule (Glisson's capsule, yellow arrowhead, *bottom*) was isolated from normal human liver tissue to visualize capsular lymphatic vessels. *D*, *left*: reconstructed 3-D image of lymphatic vessels (PDPN, red) in the capsular area of normal human liver tissue. Imaging condition: z-step size = 0.3 μm, image volume $[x] \times [y] \times [z] = 1{,}551\ \mu m \times 1{,}551\ \mu m \times 145\ \mu m$. Scale bars: 100 μm. *Right*: 3-D volume-rendering image. Scale bars: 100 μm.

measurements of lymphatic vessel area in 2-D and volume in 3-D. On average, the area of lymphatic vessels was 2.1 times larger in BDL livers than sham livers ($P = 0.015$, $14.1 \pm 2.0 \times 10^2\ \mu m^2$ vs. $6.7 \pm 1.6 \times 10^2\ \mu m^2$). In comparison, 3-D volumetric analysis of lymphatic vessels showed a 4.3-fold increase in the total volume in BDL livers compared with sham livers. These comparisons may indicate that 2-D analysis could underestimate the magnitude of lymphatic vascular alterations in liver disease, and that 3-D analysis may provide a more accurate and in-depth evaluation of the architecture of lymphatic vessels.

DISCUSSION

Using our modified CUBIC tissue-clearing method, we showed the detailed architecture of lymphatic vessels along with bile ducts and blood vessels in the portal tract of mouse and human livers. Furthermore, 3-D volume imaging with comprehensive quantitative analysis revealed alterations in lymphatic vessel structure with increased diameters and branch numbers in mouse biliary fibrotic livers. Our optimized tissue-clearing method allows detailed analysis of lymphatic vessels as well as bile ducts and blood

Downloaded from journals.physiology.org/journal/ajpgi (172.232.036.207) on November 21, 2025.

vessels in normal and diseased livers in rodents and humans.

Hyperhydration-based tissue-clearing methods such as the CUBIC method are useful for 3-D histology, since they provide more effective delipidation with minimal damage of tissue structure (35). Particularly, tetrakis (2-hydroxyethyl) ethylenediamine in the CUBIC tissue-clearing reagent can remove hemes effectively from blood-rich organs, enabling 3-D imaging of various organs (3). In general, the CUBIC method requires immunolabeling in the middle of the tissue-clearing process after treatment with CUBIC reagent-1 and proceeds to the decolorization process with CUBIC reagent-2 to remove endogenous pigments, especially hemes (3, 5). In this procedure, however, organs with high volumes of residual blood, such as the liver, need a long tissue-clearing time with a highly concentrated detergent at a relatively high temperature, which tends to impair fluorescent signals (8). Therefore, to preserve sufficient fluorescent signals, we modified the original method by applying antibodies to fully cleared tissues after completing tissue-clearing, followed by a short time (1 day) of postimmunostaining tissue-clearing at room temperature (Fig. 1). Furthermore, we increased antibody permeability in the immunostaining process by sectioning cleared liver tissues to less than 3-mm thickness.

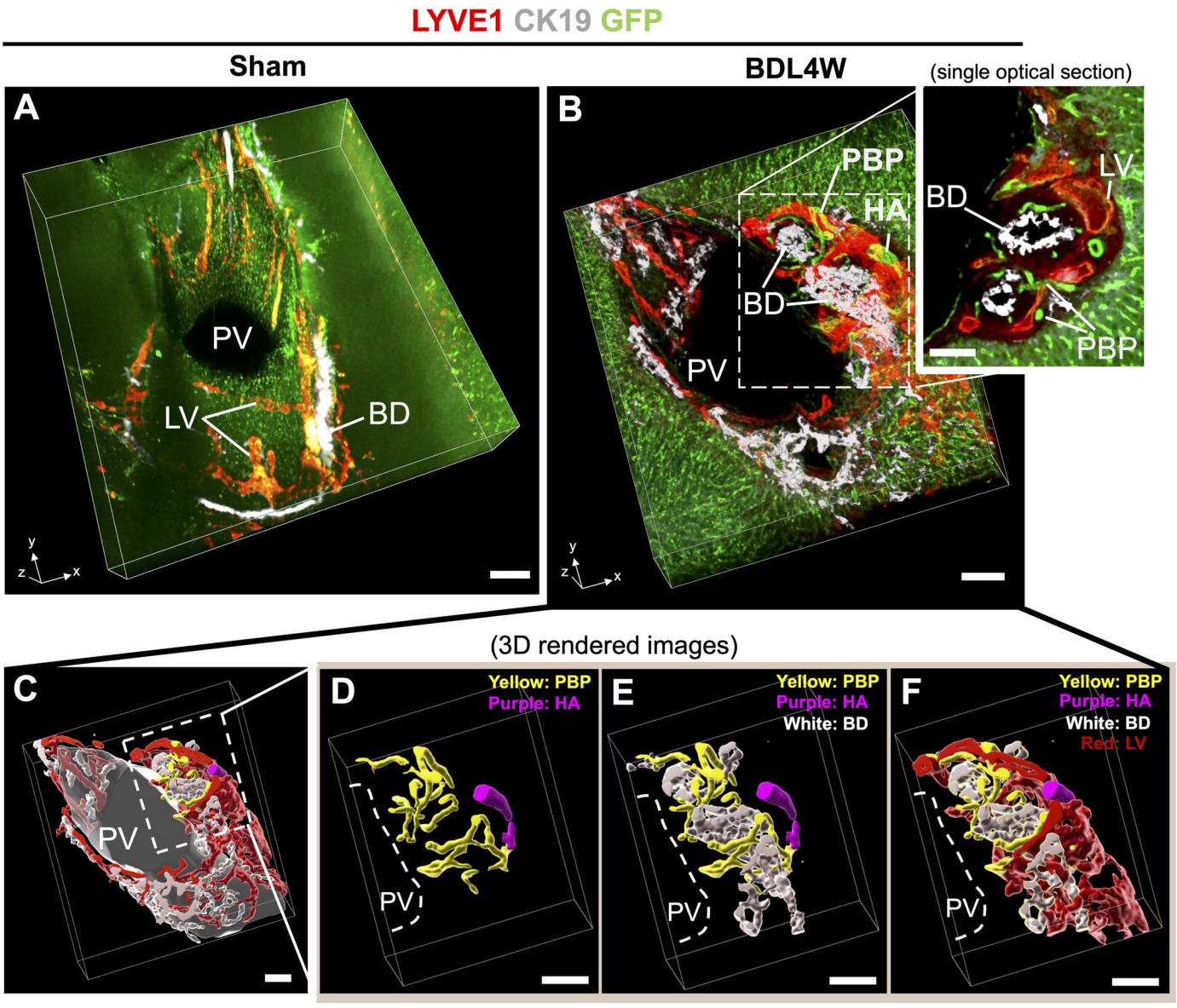

Figure 4. Spatial relationship between lymphatic vessels and bile ducts in biliary cirrhotic livers. *A*: reconstructed three-dimensional (3-D) image of the portal tract in the liver from a sham-operated mouse (EC-GFP reporter mouse). Imaging condition: *z*-step size = 0.4 μm, image volume [*x*] × [*y*] × [*z*] = 1,025 μm × 1,161 μm × 211 μm. Liver tissue was cleared and stained with LYVE1 (red, lymphatic vessel: LV) and CK19 (white, bile duct: BD). Scale bar: 100 μm. *B*: reconstructed 3-D image of the portal tract in the liver from a 4-wk BDL mouse (EC-GFP reporter mouse) with a representative single optical section in the *right*. Imaging condition: *z*-step size = 0.4 μm, image volume [*x*] × [*y*] × [*z*] = 862 μm × 939 μm × 220 μm. Liver tissue was cleared and stained with LYVE1 (red, lymphatic vessel) and CK19 (white, bile duct). LV, lymphatic vessel; BD, bile duct; PV, portal vein; HA, hepatic artery; PBP: peribiliary plexus. Scale bars: 100 μm. *C*: 3-D volume-rendering image of lymphatic vessels and bile ducts in the portal tract with enlarged images (*D*–*F*). Scale bar: 100 μm. BDL, bile duct ligation; EC-GFP, Endothelial-specific green fluorescent protein mice; LV, lymphatic vessel.

Downloaded from journals.physiology.org/journal/ajpgi (172.232.036.207) on November 21, 2025.

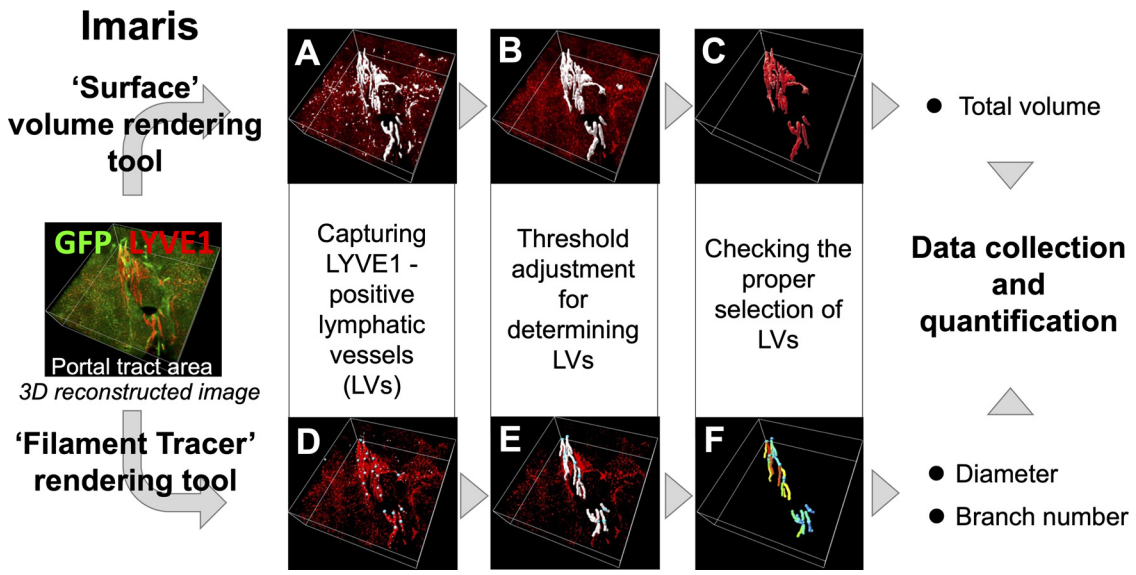

Figure 5. A workflow for quantification of lymphatic vessel parameters in 3-D volume images. Cleared liver tissue was stained with LYVE1 (red) for lymphatic vessels (LVs) and reconstructed three-dimensional (3-D) images of the portal tract in the mouse liver (EC-GFP reporter mouse) were created. The "Surface" rendering tool in Imaris software were used to determine a total volume of LYVE1-positive LVs (*A*–*C*), whereas the "Filament Tracer" rendering tool was used for quantification of the diameter and branch number of LVs (*D*–*F*). *A*:LYVE1-positive LVs were captured based on fluorescence intensities. *B*: thresholds were manually adjusted to determine LVs. *C*:Rendered LYVE1-positive LVs were visually checked to confirm proper vascular connections. LVs with improper connections and/or speckled background structure were removed manually. *D*: LYVE1-positive LVs were captured based on fluorescence intensities using automatic filament and path detection in the "Filament Tracer" rendering tool. *E*: thresholds were manually adjusted to determine LVs. *F*: LVs with disconnected and speckled background structures were removed manually. All outputs of LV parameters were exported to Excel files for statistical analysis. EC-GFP, Endothelial-specific green fluorescent protein mice; LV, lymphatic vessel.

These modifications can easily be adopted in any standard laboratory environment to attain a reasonable scale of 3-D visualization.

We also investigated lymphatic vessels in the liver capsular area, including the first 3-D volume images of a well-structured capsular lymphatic network in normal human livers. Lymphatic vessels in the liver are mostly found in the portal tract (36), managing around 80% of the lymph produced by the liver, while the remaining lymph is drained into lymphatic vessels in the capsular area (1). Unlike in human liver tissue, however, we were not able to identify capsular lymphatic vessels in normal mouse or rat livers under the 3-D volumetric projection or in 2-D conventional histological analysis (Fig. 3*B*). We postulate this difference in the number of capsular lymphatics may be due to differences in organ sizes or structural characteristics between human and rodent livers. The liver capsular area (Glisson's capsule) tends to be thicker in larger animals (37), which is consistent with our observation (Fig. 3*A*) that the liver capsular area was significantly thicker in humans than in mice or rats (12.5-fold and 9.8-fold, respectively). In the normal human liver, the capsular area consists of multilayers of capsular fibroblasts in thick collagenous connective tissue beneath the mesothelium (37). Compared with the human liver, the collagenous connective tissue of Glisson's capsule in the normal mouse liver is underdeveloped beneath the liver surface (a single layer of capsular fibroblasts) (37, 38). The richness of the collagenous matrix in the capsular area may account for the massive development of capsular lymphatics in humans because the adhesion of lymphatic endothelial cells to the extracellular matrix (ECM, e.g., collagen) activates B1 integrin signaling, which promotes lymphangiogenesis by c-Src-dependent VEGFR-3 phosphorylation in the absence of VEGFR3 ligands (39). Further, ECM proteins such as collagen, laminin, and fibronectin also provide a mechanical link between the ECM and the cytoskeleton, anchoring lymphatic endothelial cells and supporting lymphatic morphogenesis (40). By contrast, an underdeveloped ECM bed in rodent liver capsule may not work well for lymphangiogenesis. The differences in the capsular lymphatic network between humans and rodents may indicate possible differences in the function of the liver lymphatic system between these species.

Structural changes in hepatic lymphatic vessels have not been well characterized. Using 3-D volume images of cleared liver sections attained with our modified CUBIC method, we were able to evaluate structural alterations of liver lymphatics in a mouse model of biliary fibrosis (BDL). In the normal liver, lymphatic vessels mostly ran alongside bile ducts in the portal tract, while in the biliary fibrotic liver, increased, dilated lymphatic vessels with elongated branches surrounded bile ducts and peribiliary vascular plexuses (PBPs). These observations are consistent with quantification data of increased lymphatic vessel densities in the portal tract reported for patients with primary biliary cholangitis (41), presenting evidence for extensive remodeling and expansion of the lymphatic vasculature occurring in biliary fibrotic livers. In addition, a comparison of the quantification of lymphatic vessel areas in the portal tract between fragmented images (2-D) and volume images (3-D) demonstrated that changes of the lymphatic vessel total volume in BDL livers in 3-D (4.3-fold) were remarkably larger than changes of the lymphatic vessel total area determined in 2-D (2.1-fold). All these observations may indicate that our 3-D volumetric analysis could detect dynamic remodeling of the lymphatic vasculature due to liver diseases more comprehensively.

Downloaded from journals.physiology.org/journal/ajpgi (172.232.036.207) on November 21, 2025.

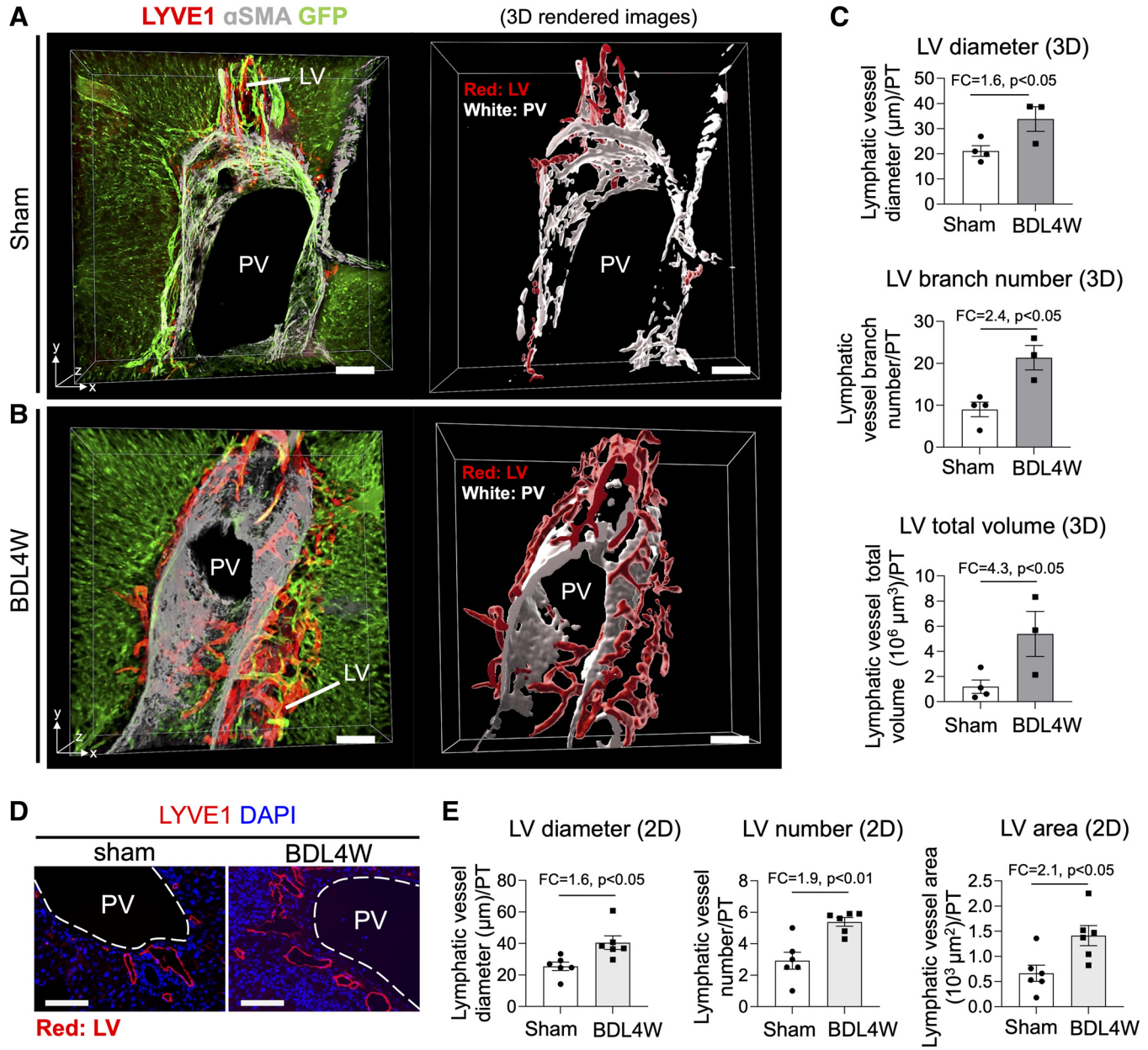

Figure 6. Comparison of lymphatic vessel parameters between 3-D volume-rendering images and conventional two-dimensional (2-D) images in normal and biliary fibrotic livers. *A*, *left*: reconstructed three-dimensional (3-D) image of the portal tract in the liver from a sham-operated mouse (EC-GFP reporter mouse). Imaging condition: *z*-step size = 0.4 μm step, image volume [*x*] × [*y*] × [*z*] = 777 μm × 777 μm × 215 μm. Liver tissue was cleared and stained with LYVE1 (red, lymphatic vessel: LV) and αSMA (white, portal vein: PV). *Right*: 3-D volume-rendering image of lymphatic vessels and portal vein using Imaris software. Scale bars: 100 μm. *B*, *left*: reconstructed 3-D image of the portal tract in the liver from a 4-wk BDL mouse (EC-GFP reporter mouse). Imaging condition: *z*-step size = 0.4 μm, image volume [*x*] × [*y*] × [*z*] = 793 μm × 894 μm × 190 μm. *Right*: 3-D volume-rendering image of lymphatic vessels and portal vein using Imaris software. Scale bars: 100 μm. *C*: quantification of lymphatic vessel (LV) parameters (diameter, branch number, and total volume) from 3-D volume-rendering images in sham ($n = 4$) and 4-wk BDL ($n = 3$) mouse livers. PT, portal tract; FC, fold change. *D*: conventional 2-D images of liver tissues (frozen section, 7-μm thickness) from sham and 4-wk BDL mice (EC-GFP reporter mice). Red: LYVE1-positive lymphatic vessel. Scale bars: 100 μm. *E*: quantification of LV parameters (diameter, number, and total area) from conventional 2-D images in sham ($n = 6$) and 4-wk BDL ($n = 6$) mouse livers. BDL, bile duct ligation; EC-GFP, Endothelial-specific green fluorescent protein mice; LV, lymphatic vessel.

Biliary diseases or cholangiopathies are a group of chronic liver diseases characterized by highly proliferating cholangiocytes and progressive biliary fibrosis. Proliferative responses of cholangiocytes are regulated by a complex interaction involving various autocrine or paracrine factors (42). It is reported that cholangiocytes secret angiogenic factors (e.g., vascular endothelial growth factors, VEGFs), leading to the expansion of peribiliary vascular plexuses (PBPs) or small hepatic arteries. However, the effects of proliferating cholangiocytes on liver lymphangiogenesis are largely unknown. Our 3-D volumetric analysis revealed that bile ducts and PBPs were dramatically increased in BDL 4-wk mouse livers and that increased biliary ductal reaction areas were prominently surrounded by increased and dilated lymphatic vessels. These

Downloaded from journals.physiology.org/journal/ajpgi (172.232.036.207) on November 21, 2025.

observations may suggest a spatial clue to the involvement of cholangiocytes in lymphangiogenesis (Fig. 4). In addition, several studies reported that proliferating cholangiocytes could express VEGF-C, a potent lymphangiogenic factor (43).

This study did not present the whole-liver lymphatic vasculature but instead focused on the lymphatic vasculature enriched areas (portal tract and capsular areas) due to the limitation of the imaging depth taken by a conventional confocal microscope. For a more complete understanding of hepatic lymphatics in 3-D, particularly for diseased livers, imaging the whole liver would be ideal. To this end, advanced microscopic technologies, such as light sheet fluorescence microscopy (LSFM), can be used along with our modified CUBIC tissue-clearing method. LSFM can scan images with high speeds and high resolutions, minimizing photobleaching and allowing more efficient illumination for large tissue sections.

In conclusion, we have demonstrated a simple modified CUBIC method for both human and rodent liver tissue-clearing. The modified CUBIC method in combination with effective immunolabeling enabled us to visualize hepatic lymphatics along with blood vessels and bile ducts in 3-D and quantify lymphatic vessels thoroughly, helping to fully evaluate their structural alterations in a mouse model of biliary fibrosis. This approach can be used to characterize lymphatics or other vasculatures in a wide range of liver disease conditions in both humans and rodent models.

SUPPLEMENTAL DATA

Supplemental Video S1 and extended procedure files: https://doi.org/10.5281/zenodo.8124940.

ACKNOWLEDGMENTS

The authors sincerely thank all the deceased organ donors and their families for their generous gifts to enable this work. The authors also thank New England Donor Services for their assistance and dedication in obtaining deceased donor organs for research.

GRANTS

This work was funded by National Institute of Diabetes and Digestive and Kidney Diseases Grants R56DK121511 and R01DK121511 (to Y.I.); Department of Defense Grant W81XWH1810184 (to Y.I.); and National Institute on Alcohol Abuse and Alcoholism Grant K08AA029182 (to M.J.M.).

DISCLOSURES

No conflicts of interest, financial or otherwise, are declared by the authors.

AUTHOR CONTRIBUTIONS

J.J., M.T., T.U., and Y.I. conceived and designed research; J.J., M.T., Y.Y., N.A., J.D., and T.U. performed experiments; J.J. and N.A. analyzed data; J.J., N.A., and Y.I. interpreted results of experiments; J.J. and N.A. prepared figures; J.J. and N.A. drafted manuscript; J.J., Y.Y., G.T., X.Z., M.J.M., T.U., and Y.I. edited and revised manuscript; J.D., G.T., X.Z., T.U., and Y.I. approved final version of manuscript.

REFERENCES

1. **Jeong J**, **Tanaka M**, **Iwakiri Y.** Hepatic lymphatic vascular system in health and disease. *J Hepatol* 77: 206–218, 2022. doi:10.1016/j.jhep.2022.01.025.
2. **Chung C**, **Iwakiri Y.** The lymphatic vascular system in liver diseases: its role in ascites formation. *Clin Mol Hepatol* 19: 99–104, 2013. doi:10.3350/cmh.2013.19.2.99.
3. **Susaki EA**, **Tainaka K**, **Perrin D**, **Kishino F**, **Tawara T**, **Watanabe TM**, **Yokoyama C**, **Onoe H**, **Eguchi M**, **Yamaguchi S**, **Abe T**, **Kiyonari H**, **Shimizu Y**, **Miyawaki A**, **Yokota H**, **Ueda HR.** Whole-brain imaging with single-cell resolution using chemical cocktails and computational analysis. *Cell* 157: 726–739, 2014. doi:10.1016/j.cell.2014.03.042.
4. **Susaki EA**, **Tainaka K**, **Perrin D**, **Yukinaga H**, **Kuno A**, **Ueda HR.** Advanced CUBIC protocols for whole-brain and whole-body clearing and imaging. *Nat Protoc* 10: 1709–1727, 2015. doi:10.1038/nprot.2015.085.
5. **Nojima S**, **Susaki EA**, **Yoshida K**, **Takemoto H**, **Tsujimura N**, **Iijima S**, **Takachi K**, **Nakahara Y**, **Tahara S**, **Ohshima K**, **Kurashige M**, **Hori Y**, **Wada N**, **Ikeda J-I**, **Kumanogoh A**, **Morii E**, **Ueda HR.** CUBIC pathology: three-dimensional imaging for pathological diagnosis. *Sci Rep* 7: 9269, 2017. doi:10.1038/s41598-017-09117-0.
6. **Fumoto S**, **Nishimura K**, **Nishida K**, **Kawakami S.** Three-dimensional imaging of the intracellular fate of plasmid DNA and transgene expression: ZsGreen1 and tissue clearing method CUBIC are an optimal combination for multicolor deep imaging in murine tissues. *PLoS One* 11: e0148233, 2016. doi:10.1371/journal.pone.0148233.
7. **Liu L**, **Xia X**, **Xiang F**, **Gao Y**, **Li X**, **Li H**, **Zheng W.** F-CUBIC: a rapid optical clearing method optimized by quantitative evaluation. *Biomed Opt Express* 13: 237–251, 2022. doi:10.1364/BOE.442976.
8. **Xu J**, **Ma Y**, **Yu T**, **Zhu D.** Quantitative assessment of optical clearing methods in various intact mouse organs. *J Biophotonics* 12: e201800134, 2019. doi:10.1002/jbio.201800134.
9. **Qi Y**, **Yu T**, **Xu J**, **Wan P**, **Ma Y**, **Zhu J**, **Li Y**, **Gong H**, **Luo Q**, **Zhu D.** FDISCO: advanced solvent-based clearing method for imaging whole organs. *Sci Adv* 5: eaau8355, 2019. doi:10.1126/sciadv.aau8355.
10. **Pitulescu ME**, **Schmidt I**, **Benedito R**, **Adams RH.** Inducible gene targeting in the neonatal vasculature and analysis of retinal angiogenesis in mice. *Nat Protoc* 5: 1518–1534, 2010. doi:10.1038/nprot.2010.113.
11. **Li J**, **Li E**, **Czepielewski RS**, **Chi J**, **Guo X**, **Han YH**, **Wang D**, **Wang L**, **Hu B**, **Dawes B**, **Jacobs C**, **Tenen D**, **Lin SJ**, **Lee B**, **Morris D**, **Tobias A**, **Randolph GJ**, **Cohen P**, **Tsai L**, **Rosen ED.** Neurotensin is an antithermogenic peptide produced by lymphatic endothelial cells. *Cell Metab* 33: 1449–1465.e6, 2021. doi:10.1016/j.cmet.2021.04.019.
12. **Ikeda S**, **Sugioka S**, **Kimura T**, **Ashida N.** Smooth muscle protein 22α-Cre recombination in resting cardiac fibroblasts and hematopoietic precursors. *Sci Rep* 12: 11564, 2022 [Erratum in *Sci Rep* 12: 22026, 2022]. doi:10.1038/s41598-022-15957-2.
13. **Qiu Q**, **Hernandez JC**, **Dean AM**, **Rao PH**, **Darlington GJ.** CD24-positive cells from normal adult mouse liver are hepatocyte progenitor cells. *Stem Cells Dev* 20: 2177–2188, 2011. doi:10.1089/scd.2010.0352.
14. **Yang P**, **Wang Y**, **Tang W**, **Sun W**, **Ma Y**, **Lin S**, **Jing J**, **Jiang L**, **Shi H**, **Song Z**, **Yu L.** Western diet induces severe nonalcoholic steatohepatitis, ductular reaction, and hepatic fibrosis in liver CGI-58 knockout mice. *Sci Rep* 10: 4701, 2020. doi:10.1038/s41598-020-61473-6.
15. **Gibot L**, **Galbraith T**, **Bourland J**, **Rogic A**, **Skobe M**, **Auger FA.** Tissue-engineered 3D human lymphatic microvascular network for in vitro studies of lymphangiogenesis. *Nat Protoc* 12: 1077–1088, 2017. doi:10.1038/nprot.2017.025.
16. **Guo Q**, **Furuta K**, **Islam S**, **Caporarello N**, **Kostallari E**, **Dielis K**, **Tschumperlin DJ**, **Hirsova P**, **Ibrahim SH.** Liver sinusoidal endothelial cell expressed vascular cell adhesion molecule 1 promotes liver fibrosis. *Front Immunol* 13: 983255, 2022. doi:10.3389/fimmu.2022.983255.
17. **Tai-Nagara I**, **Hasumi Y**, **Kusumoto D**, **Hasumi H**, **Okabe K**, **Ando T**, **Matsuzaki F**, **Itoh F**, **Saya H**, **Liu C**, **Li W**, **Mukouyama YS**, **Marston Linehan W**, **Liu X**, **Hirashima M**, **Suzuki Y**, **Funasaki S**, **Satou Y**, **Furuya M**, **Baba M**, **Kubota Y.** Blood and lymphatic systems are segregated by the FLCN tumor suppressor. *Nat Commun* 11: 6314, 2020. doi:10.1038/s41467-020-20156-6.

Downloaded from journals.physiology.org/journal/ajpgi (172.232.036.207) on November 21, 2025.

18. **Brezovakova V**, **Jadhav S.** Identification of Lyve-1 positive macrophages as resident cells in meninges of rats. *J Comp Neurol* 528: 2021–2032, 2020. doi:10.1002/cne.24870.
19. **de Moraes ACN**, **de Andrade CBV**, **Ramos IPR**, **Dias ML**, **Batista CMP**, **Pimentel CF**, **de Carvalho JJ**, **Goldenberg R.** Resveratrol promotes liver regeneration in drug-induced liver disease in mice. *Food Res Int* 142: 110185, 2021. doi:10.1016/j.foodres.2021.110185.
20. **Park JK**, **Shao M**, **Kim MY**, **Baik SK**, **Cho MY**, **Utsumi T**, **Satoh A**, **Ouyang X**, **Chung C**, **Iwakiri Y.** An endoplasmic reticulum protein, Nogo-B, facilitates alcoholic liver disease through regulation of kupffer cell polarization. *Hepatology* 65: 1720–1734, 2017. doi:10.1002/hep.29051.
21. **Iwakiri Y**, **Cadelina G**, **Sessa WC**, **Groszmann RJ.** Mice with targeted deletion of eNOS develop hyperdynamic circulation associated with portal hypertension. *Am J Physiol Gastrointest Liver Physiol* 283: G1074–G1081, 2002. doi:10.1152/ajpgi.00145.2002.
22. **Abraldes JG**, **Iwakiri Y**, **Loureiro-Silva M**, **Haq O**, **Sessa WC**, **Groszmann RJ.** Mild increases in portal pressure upregulate vascular endothelial growth factor and endothelial nitric oxide synthase in the intestinal microcirculatory bed, leading to a hyperdynamic state. *Am J Physiol Gastrointest Liver Physiol* 290: G980–G987, 2006. doi:10.1152/ajpgi.00336.2005.
23. **Hsu SJ**, **Zhang C**, **Jeong J**, **Lee SI**, **McConnell M**, **Utsumi T**, **Iwakiri Y.** Enhanced meningeal lymphatic drainage ameliorates neuroinflammation and hepatic encephalopathy in cirrhotic rats. *Gastroenterology* 160: 1315–1329.e13, 2021. doi:10.1053/j.gastro.2020.11.036.
24. **Huang HC**, **Haq O**, **Utsumi T**, **Sethasine S**, **Abraldes JG**, **Groszmann RJ**, **Iwakiri Y.** Intestinal and plasma VEGF levels in cirrhosis: the role of portal pressure. *J Cell Mol Med* 16: 1125–1133, 2012. doi:10.1111/j.1582-4934.2011.01399.x.
25. **Lee CH**, **Loureiro-Silva MR**, **Abraldes JG**, **Iwakiri Y**, **Haq O**, **Groszmann RJ.** Decreased intrahepatic response to α_1-adrenergic agonists in lipopolysaccharide-treated rats is located in the sinusoidal area and depends on Kupffer cell function. *J Gastroenterol Hepatol* 22: 893–900, 2007. doi:10.1111/j.1440-1746.2007.04922.x.
26. **Loureiro-Silva MR**, **Cadelina GW**, **Iwakiri Y**, **Groszmann RJ.** A liver-specific nitric oxide donor improves the intra-hepatic vascular response to both portal blood flow increase and methoxamine in cirrhotic rats. *J Hepatol* 39: 940–946, 2003. doi:10.1016/j.jhep.2003.09.018.
27. **Park JK**, **Utsumi T**, **Seo YE**, **Deng Y**, **Satoh A**, **Saltzman WM**, **Iwakiri Y.** Cellular distribution of injected PLGA-nanoparticles in the liver. *Nanomedicine* 12: 1365–1374, 2016. doi:10.1016/j.nano.2016.01.013.
28. **Su T**, **Yang Y**, **Lai S**, **Jeong J**, **Jung Y**, **McConnell M**, **Utsumi T**, **Iwakiri Y.** Single-cell transcriptomics reveals zone-specific alterations of liver sinusoidal endothelial cells in cirrhosis. *Cell Mol Gastroenterol Hepatol* 11: 1139–1161, 2021. doi:10.1016/j.jcmgh.2020.12.007.
29. **Tsai MH**, **Iwakiri Y**, **Cadelina G**, **Sessa WC**, **Groszmann RJ.** Mesenteric vasoconstriction triggers nitric oxide overproduction in the superior mesenteric artery of portal hypertensive rats. *Gastroenterology* 125: 1452–1461, 2003. doi:10.1016/j.gastro.2003.07.014.
30. **Yang Y**, **Sangwung P**, **Kondo R**, **Jung Y**, **McConnell MJ**, **Jeong J**, **Utsumi T**, **Sessa WC**, **Iwakiri Y.** Alcohol-induced Hsp90 acetylation is a novel driver of liver sinusoidal endothelial dysfunction and alcohol-related liver disease. *J Hepatol* 75: 377–386, 2021. doi:10.1016/j.jhep.2021.02.028.
31. **Zhang D**, **Utsumi T**, **Huang HC**, **Gao L**, **Sangwung P**, **Chung C**, **Shibao K**, **Okamoto K**, **Yamaguchi K**, **Groszmann RJ**, **Jozsef L**, **Hao Z**, **Sessa WC**, **Iwakiri Y.** Reticulon 4B (Nogo-B) is a novel regulator of hepatic fibrosis. *Hepatology* 53: 1306–1315, 2011. doi:10.1002/hep.24200.
32. **Schoenfeld DA.** Sample-size formula for the proportional-hazards regression model. *Biometrics* 39: 499–503, 1983.
33. **Tag CG**, **Sauer-Lehnen S**, **Weiskirchen S**, **Borkham-Kamphorst E**, **Tolba RH**, **Tacke F**, **Weiskirchen R.** Bile duct ligation in mice: induction of inflammatory liver injury and fibrosis by obstructive cholestasis. *J Vis Exp* 96: 52438, 2015. doi:10.3791/52438.
34. **Maroni L**, **Haibo B**, **Ray D**, **Zhou T**, **Wan Y**, **Meng F**, **Marzioni M**, **Alpini G.** Functional and structural features of cholangiocytes in health and disease. *Cell Mol Gastroenterol Hepatol* 1: 368–380, 2015. doi:10.1016/j.jcmgh.2015.05.005.
35. **Tainaka K**, **Kuno A**, **Kubota SI**, **Murakami T**, **Ueda HR.** Chemical principles in tissue clearing and staining protocols for whole-body cell profiling. *Annu Rev Cell Dev Biol* 32: 713–741, 2016. doi:10.1146/annurev-cellbio-111315-125001.
36. **Tanaka M**, **Iwakiri Y.** The Hepatic Lymphatic Vascular System: Structure, Function, Markers, and Lymphangiogenesis. *Cell Mol Gastroenterol Hepatol* 2: 733–749, 2016. doi:10.1016/j.jcmgh.2016.09.002.
37. **Balog S**, **Li Y**, **Ogawa T**, **Miki T**, **Saito T**, **French SW**, **Asahina K.** Development of capsular fibrosis beneath the liver surface in humans and mice. *Hepatology* 71: 291–305, 2020. doi:10.1002/hep.30809.
38. **Kendall RT**, **Feghali-Bostwick CA.** Fibroblasts in fibrosis: novel roles and mediators. *Front Pharmacol* 5: 123, 2014. doi:10.3389/fphar.2014.00123.
39. **Galvagni F**, **Pennacchini S**, **Salameh A**, **Rocchigiani M**, **Neri F**, **Orlandini M**, **Petraglia F**, **Gotta S**, **Sardone GL**, **Matteucci G**, **Terstappen GC**, **Oliviero S.** Endothelial cell adhesion to the extracellular matrix induces c-Src-dependent VEGFR-3 phosphorylation without the activation of the receptor intrinsic kinase activity. *Circ Res* 106: 1839–1848, 2010. doi:10.1161/CIRCRESAHA.109.206326.
40. **Wiig H**, **Keskin D**, **Kalluri R.** Interaction between the extracellular matrix and lymphatics: consequences for lymphangiogenesis and lymphatic function. *Matrix Biol* 29: 645–656, 2010. doi:10.1016/j.matbio.2010.08.001.
41. **Yamauchi Y**, **Ikeda R**, **Michitaka K**, **Hiasa Y**, **Horiike N**, **Onji M.** Morphometric analysis of lymphatic vessels in primary biliary cirrhosis. *Hepatol Res* 24: 107, 2002. doi:10.1016/s1386-6346(02)00019-0.
42. **Glaser SS**, **Gaudio E**, **Miller T**, **Alvaro D**, **Alpini G.** Cholangiocyte proliferation and liver fibrosis. *Expert Rev Mol Med* 11: e7, 2009. doi:10.1017/S1462399409000994.
43. **Gaudio E**, **Barbaro B**, **Alvaro D**, **Glaser S**, **Francis H**, **Ueno Y**, **Meininger CJ**, **Franchitto A**, **Onori P**, **Marzioni M**, **Taffetani S**, **Fava G**, **Stoica G**, **Venter J**, **Reichenbach R**, **De Morrow S**, **Summers R**, **Alpini G.** Vascular endothelial growth factor stimulates rat cholangiocyte proliferation via an autocrine mechanism. *Gastroenterology* 130: 1270–1282, 2006. doi:10.1053/j.gastro.2005.12.034.

Downloaded from journals.physiology.org/journal/ajpgi (172.232.036.207) on November 21, 2025.